A Time Resolved Static Light Scattering Study on Nucleation and Crystallization in a Colloidal System

JAN K. G. DHONT,[1] CARLA SMITS, AND HENK N. W. LEKKERKERKER

Van 't Hoff Laboratorium voor Fysische en Colloidchemie, University of Utrecht, Padualaan 8, 3584 CH Utrecht, The Netherlands

Received September 11, 1991; accepted December 10, 1991

The crystallization process in a colloidal system of slightly charged spherical particles is studied with time-resolved static light scattering. The induction time, the crystallization rate, the scattered intensity after completion of the crystallization process, and the width of the Bragg peaks are found to be strongly dependent on the concentration of the initially metastable colloidal fluid. Assuming a simple crystal geometry, quantities such as the size of the crystallites, the number concentration of the crystallites, and nucleation and crystallite growth rates, as functions of the concentration, are calculated from these experimental quantities.

1. INTRODUCTION

Crystallization of colloidal systems has mostly been investigated in aqueous dispersions of highly charged colloidal particles. Hachisu and Takano (1) constructed a phase diagram of aqueous polystyrene dispersions. They observed a disorder-to-order phase separation on increasing the concentration which they relate to the Kirkwood–Alder transition (2, 3). Another comprehensive phase diagram for charged particles has been described by Monovoukas and Gast (4). Besides a disorder-to-order transition, they also observed a transition from body centered cubic (BCC) to face centered cubic (FCC). Usually BCC is only formed in dilute samples (with volume fractions $\phi < 0.02$) and FCC is formed for higher volume fractions (approximately $\phi > 0.03$). These charged colloidal particles have a long range of interaction and can crystallize at low volume fractions. Crystallization generally occurs in a few minutes or even faster, but slower crystallization may also be observed.

Pusey and Van Megen (5, 6) performed similar experiments with (nearly) hard sterically stabilized particles. With increasing concentration of the particles, the following structures are observed: liquid-like structures, coexistence of a liquid with a crystal, fully crystalline structures, and glassy states. Crystal structures are FCC or FCC/HCP mixtures.

Besides this structural information, it is interesting to look at the kinetics of crystallization. Qualitative observations and crude quantitative experiments showed that the rate of crystal formation as a function of the concentration exhibits a maximum at the melting concentration. The size of the crystallites was seen to decrease with increasing concentration, but in the coexistence region, where significant sedimentation occurs during the crystallization process, the crystallites appeared to have similar sizes independent of the concentration (5, 6). Other experiments on the kinetics of the crystallization process have been performed by Aastuen *et al.* (7), on highly charged polystyrene spheres, and by Davis and Russel (8), on dilute sedimenting hard-sphere dispersions. Cape *et al.* (9) describe computer simulations on the structure of the various

[1] To whom correspondence should be addressed.

0021-9797/92 $5.00

nuclei that can be formed in an atomic soft sphere system. Nuclei were found to have different structures and sizes, and in the region in the phase diagram where homogeneous crystallization occurred, there seemed to be no significant energetic barrier for nucleation, so that the translational diffusional properties of the system are predicted to be nucleation rate determining. Russel (10, 11) recently adapted classical nucleation and growth theories to describe the crystallization phenomena in colloidal dispersions.

The above mentioned work on the kinetics of the nucleation/crystallization process will be discussed later in more detail, in relation to the experiments that are presented in the present paper.

We describe experiments performed with a static light-scattering setup with high angular and time resolution. With this apparatus it has become possible to study various details of the nucleation/crystallization process in colloidal systems.

In Section 2 we describe the colloidal system, its phase behaviour, and sample preparation. The light-scattering setup is explained in Section 3. In Section 4 experimental results on the kinetics of nucleation/crystal growth and the final size of the crystallites as functions of the concentration are presented. Calculations of quantities that characterize the nucleation/crystal growth kinetics, based on the experimental data, are given in Section 5. Finally, in Section 6, the results are discussed and compared with earlier work.

2. THE COLLOIDAL SYSTEM, ITS PHASE DIAGRAM, AND SAMPLE PREPARATION

The colloidal system used in the experiments consists of silica particles, stabilized with γ-methacryloxypropyltrimethoxysilane. The synthesis of these particles (hereafter referred to as TPM-particles or TPM-silica) is described in Ref. (12). The solvent is a mixture of toluene and ethanol, such that the refractive index equals 1.4490 ± 0.0001. The particles are almost perfectly refractive index-matched in this solvent (approximately up to a few digits in the third decimal place). The refractive index of the solvent was monitored during the experiments. To this end, the refractive indices of the supernatants of centrifuged samples were measured several times. It is important to keep the refractive index of the solvent fixed (up to a few digits in the fourth decimal place) since the scattered intensity is quite sensitive to the refractive index of the solvent as the result of its close match to the refractive index of the TPM-particles.

The hydrodynamic radius of the silica core of the particles as measured with dynamic light-scattering on the alcosol is 160 nm. The hydrodynamic radius of the TPM-particles, measured in a slightly refractive index-mismatched solvent through a slight change of the toluene/ethanol composition, is 2 to 4 nm larger; this is an indication of the thickness of the surface coating of the particles. The relative standard deviation in the radius of the particles, as measured with transmission electron microscopy, is 6%.

The TPM-particles are slightly negatively charged due to the dissociation of the acid silanol groups on the particles' silica-core surface and of the acid silanol groups of the TPM-oligomers, attached to the surface (12). Electrophoretic mobility measurements were performed on a dilute dispersion (0.018 g/ml) in order to determine the surface charge and the Debye screening length of the particles. These measurements were done with a Pen Kem 3000 (Pen Kem, Inc., New York). The electrophoretic mobility we find is (4.59 ± 0.25) $\times 10^{-9}$ m^2/V s.

In the range of values $1 < \kappa a < 30$ and $0.5 < u_E 3\eta e/2\epsilon kT < 2.5$, the following relation between the electrophoretic mobility u_E and the zeta potential ζ holds to within about 5 mV accuracy for ζ (13),

$$u_E = \frac{2\epsilon\zeta}{3\eta} f(\kappa a), \qquad [2.1]$$

where $f(x)$ is a function that increases from 1.027 to 1.133 for x increasing from 1 to 4.

Here ϵ is the dielectric constant of the solvent, η is the viscosity of the solvent, κ is the inverse Debye screening length, and a is the hard-core radius of the Brownian particles. Furthermore, in the above inequalities, k is the Boltzmann constant, $e > 0$ is the electronic charge, and T is the temperature.

Since the charge on the TPM-particles is in part located on the TPM-coating of 2–4 nm thickness, it is not a bad approximation to set the zeta potential ζ equal to the surface potential ψ.

The relation between the surface potential ψ and the surface charge Q of the particles is (14)

$$Q = 4\pi a\epsilon \frac{kT}{e} \kappa a \left[2 \sinh\left(\frac{\psi e}{2kT}\right) + \frac{4}{\kappa a} \tanh\left(\frac{\psi e}{4kT}\right)\right]. \quad [2.2]$$

In order to calculate the surface potential and the charge from [2.1] and [2.2], using the experimentally obtained electrophoretic mobility, the Debye screening length needs to be known. Since the function f in [2.1] is not very sensitive to the precise value of κa in the range pertaining to our system, an estimate of the latter is sufficient to obtain a fairly accurate value for the surface potential and the charge per particle.

The concentration of the H^+-ions in the solvent which dissociated from the TPM-particle surfaces, c_P, is related to the volume fraction ϕ of Brownian particles through

$$c_P[\text{ions/m}^3] = \frac{1}{1-\phi} \frac{3\phi}{4\pi a^3} \frac{Q}{e}. \quad [2.3]$$

Using 1.75 g/ml for the specific weight of the silica cores of the TPM-particles, the volume fraction for the sample for which the electrophoretic mobility and the conductivity is measured is found to be 0.010. For 500 elementary charges on the surface of a single TPM-particle, c_P is then found from [2.3] to be as small as 5×10^{-7} mol/dm^3. We find later that the number of elementary charges on the surface of a single particle is less than 500. The Debye length κ^{-1} will therefore be determined, at this low volume fraction, by the concentration of electrolyte that is present in the pure solvent. The solvent used here is the same as that in Ref. (15), where the Debye length was estimated to be 60 nm. Using this value for the Debye screening length in [2.1] (corresponding to a value of the function f of 1.09) gives $\psi = \zeta = 55$ mV and from [2.2] we then find $Q = 260$ elementary charges per particle. As will be discussed below, the volume fraction at which crystallization occurs is about 0.2. At this concentration of TPM-particles, the counterions will contribute to the Debye screening length, together with the electrolyte that is present in the pure solvent. The Debye screening length can now be calculated from

$$\kappa^2 = \kappa_0^2 + \frac{e^2 c_P}{\epsilon \kappa T}, \quad [2.4]$$

where $\kappa_0^{-1} = 60$ nm is the Debye screening length resulting from the electrolyte that is present in the solvent. One finds in this way $\kappa^{-1} = 43$ nm at a volume fraction of 0.2. The uncertainties in the above calculations are indicated in Table I.

TABLE I

Characteristics of the TPM-System

Solvent	64/36 (v/v) toluene/ethanol
Refractive index solvent	$n = 1.4490$
Dielectric constant solvent	$\epsilon = 10.3 \times 8.85\ 10^{-12}$ C^2/Nm^2
Viscosity solvent	$\eta = 0.8$ cP
Temperature	$T = 293.5$ K
Particle hard-core radius	$a = 160$ nm (±6%)
TPM-layer thickness	2–4 nm
Specific weight silica	1.75 g/ml
Electrophoretic mobility (at $\phi = 0.01$)	$u_E = (4.59 \pm 0.25) \times 10^{-9}$ m^2/V s
Zeta and surface potential	$\zeta = \psi = (55 \pm 10)$ mV
Elementary charges per particles	$Q = 260 \pm 60$
Debye screening length (at $\phi = 0$)	$\kappa_o^{-1} = (60 \pm 12)$ nm
Debye screening length (at $\phi = 0.2$)	$\kappa^{-1} = (43 \pm 5)$ nm

At a temperature of 20.3°C, crystallization was observed in the concentration range 0.339–0.392 g silica/ml solvent. The silica-core volume fractions can be calculated from the concentrations in g/ml by division through the (approximate) specific weight of silica, 1.75 g/ml. The silica-core volume fraction range where crystallization is observed is thus ~0.194–0.224. As is schematically depicted in Fig. 1, coexistence of a crystal and a fluid phase is seen in the concentration range 0.339–0.3440 g/ml. In this concentration range the crystals rapidly sediment over an appreciable distance during their formation. On increasing the concentration from 0.339 to 0.3440 g/ml, the part of the volume where crystals can be observed increased from zero up to about 90 percent. This hardly changed in the concentration range 0.3440–0.3800 g/ml (see Fig. 1). In this concentration range, where the crystallization process takes about a few minutes, the crystals did not sediment over a noticeable distance in a period of about one hour. The melting concentration lies somewhere in the concentration range 0.3440–0.3800 g/ml. Above 0.3800 g/ml, in addition to homogeneous crystallization, heterogeneous crystallization at the meniscus of the dispersion also occurred. Homogeneous crystallization ceases to occur above ~0.386 g/ml and only heterogeneous crystallization at the meniscus is observed. Finally, at still higher concentrations (> ~0.392 g/ml), the system does not show any crystallization over many hours and is possibly in a glassy state, although the dispersion still flows very easily.

Light-scattering experiments were done on samples with concentrations ranging from 0.3440 to 0.3800 g/ml, where crystallization is homogeneously occurring throughout the entire dispersion, and where crystallites can be observed in about 90% of the dispersion over a long period of time in comparison to the time for crystallization (see Fig. 1).

The samples were prepared as follows. First of all, dust particles were removed by centrifugation of a dilute dispersion. After transfer of the dispersion to a cylindrical 1-cm diameter cuvette, further centrifugation, decantation of excess solvent, and redispersion, a sample at a concentration larger than 0.392 g/ml is obtained. Then, by dropwise addition of solvent, a sample with a concentration of less than 0.3800 g/ml is prepared, where homogeneous crystallization into an FCC structure (or a mixture of FCC and HCP) throughout the

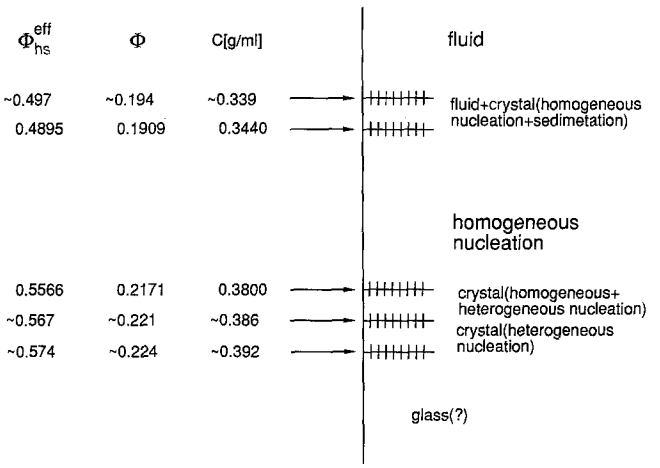

FIG. 1. Schematic phase diagram for TPM-silica at 20.3°C. The concentrations and volume fractions marked with ~ have an accuracy of about 0.0050 g/ml, the others of 0.0010 g/ml. ϕ is the volume fraction obtained from the concentration in g/ml through division by the approximate density of the particles; 1.75 g/ml. ϕ_{hs}^{eff} is the rescaled hard-sphere volume fraction (see Section 6).

dispersion is observed. After a measurement at a certain concentration, the dispersion is dropwise diluted for a subsequent measurement. The concentration is calculated from the weight of the sample. The initial, metastable fluid-like state is obtained by vigorously homogenizing the system, thereby destroying existing crystallites, by using a Vortex mixer. After the sample was mixed in this way for about 5 s, the cuvette was immediately placed in the light-scattering setup. Samples that were prepared in this way showed the same crystal growth kinetics in the entire concentration range 0.3440–0.3800 g/ml, as samples that were redispersed after centrifugation. Thus vortex mixing does destroy the crystallites and produces a truly metastable fluid. Sonification, on the other hand, was found to lead to immediate formation of nuclei/small crystallites. Existing nuclei are not destroyed by sonification.

3. THE LIGHT-SCATTERING APPARATUS AND ITS APPLICATION TO THE STUDY OF CRYSTALLIZATION KINETICS

In order to study the kinetics of crystallization, a light-scattering apparatus with a high scattering angular resolution is required. The total scattering range that is probed, however, need not be larger than a few times the width of a Bragg peak. To achieve the high angular resolution, a diode array camera of 512 pixels is positioned in the focal circle of a thermostating bath, as is schematically depicted in Fig. 2. In the experiments described here, the thermostating fluid is refractive index-matched, up to the fourth decimal place, with the dispersion. To this end we used an appropriate mixture of toluene and cyclohexane as the thermostating fluid. The radius R_F of the focal circle is then related to the radius R_T of the ring of glass surmounting the thermostating bath (GR in Fig. 2), through

$$R_F = \frac{n}{n-1} R_T, \qquad [3.1]$$

where n is the refractive index of the dispersion, c.q. the thermostating fluid. In our case $R_T = 6.50$ cm and $n = 1.4490$, so that $R_F = 20.98$ cm. In an experiment the camera diode array chip (DAC in Fig. 2) is positioned in the focal circle at the scattering peak corresponding to the (111)-Bragg peak. The width

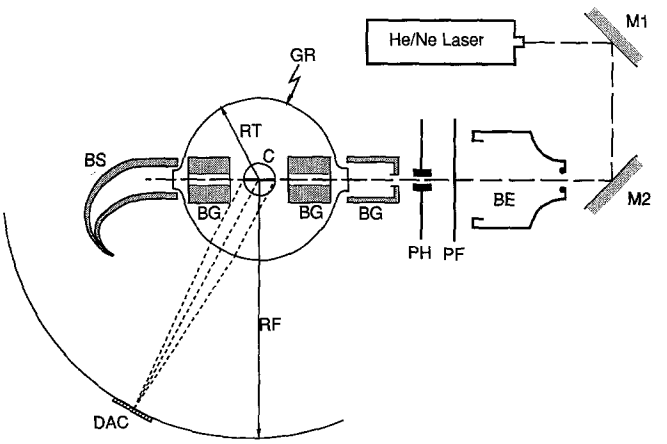

FIG. 2. The light-scattering setup. M1 and M2 are mirrors used to align the He/Ne-laser beam, BE is a beam expander, PF a polarization filter, PH a circular pinhole with a diameter that is varied from 2.4 to 6.2 mm, BG are beamguides which prevent light that is not scattered by the sample from reaching the diode array camera (DAC), BS is a beam stop, and C is a cylindrical 1-cm-diameter cuvette. The cuvette is placed in a thermostating toluene/cyclohexane bath (refractive index 1.4490) which, in part, is bounded by a ring of glass (GR). The dashed lines image scattered radiation at a particular scattering angle that is focused onto the diode array camera (DAC).

of measured Bragg peaks was indeed found to increase upon moving the camera's diode array chip away from the calculated focal circle.

The size of each pixel is 25 μm and the total length of the diode array is 512 $\times$ 25 μm = 1.28 cm, since there is no space between the diodes on the chip. The scattering angular resolution is therefore 0.007° and the total scattering angle range is 3.5°. As will be seen, this resolution and range in scattering angle perfectly fits the needs for the study of crystal growth in the TPM-silica system that is used. A beam expander (BE in Fig. 2) is used to correct the small divergence of the incident laser beam. The laser that is used is a Spectra Physics 125A He/Ne laser (the wavelength is 632 nm).

The diode array camera (EG&G, model 1452A) has a time resolution of 10 ms and a dynamic range of 2^{14}. Since crystallization in the TPM-silica system takes more than about 1 min., the time resolution is more than sufficient. In fact, since the measured scattered intensity of a crystalline sample is very much dependent on the particular configuration of the *finite* number of crystallites in the scattering volume, each experimental point in a single scattering curve is the result of many measurements which are accumulated during gentle rotation of the cuvette. The average of at least four such scattering curves is used to determine characteristic nucleation and crystal growth rate parameters. In this way the scattered intensity that is measured is the scattered intensity of crystallites averaged over all their orientations. If there is a spread in the crystallite size, the intensity is also the average over all the crystallite sizes. Several measurements were made with varying speeds of cuvette rotation. No effects on the results of an experiment were found for the typical angular rotation frequencies of about 0.01 to 0.06 Hz.

The variation of the intensity over the Debye–Scherrer ring, due to the finite number of crystallites in the scattering volume, can be decreased to some extent by increasing the scattering volume. In the experiments described here, the scattering volume was varied from $\sim$50 to 300 mm^3, by using different pinholes (PH in Fig. 2).

4. EXPERIMENTAL RESULTS

Scattered intensities are collected while rotating the sample, for reasons that were explained in the previous section. Subsequently, the orientationally averaged (111)-Bragg peak intensity thus obtained is integrated over the linear diode array. This orientationally averaged and line-integrated (111)-Bragg peak intensity I was measured as a function of time for a number of concentrations of the initially metastable fluid. In Fig. 3 a few typical curves are shown. These curves will hereafter be referred to as growth curves. From these curves three important parameters may be deduced. This is schematically depicted in Fig. 4. The slope of the curve at the inflection point is a measure for the growth rate R of the crystallites. The time after which the intensity starts to increase, the "induction time" t_i, is the time at which nuclei begin to grow. The third parameter is the "final intensity" I_f, which can be used to calculate the number concentration of crystallites. A fourth important parameter is the width of the Bragg peaks. Once these four parameters are known (as functions of the mean concentration), various other quantities can be calculated, such as the size of the crystallites, the number concentration of crystallites (c.q. nuclei), the growth rate of a single crystallite and the nucleation rate. We defer these calculations to the next section and present experimental results in this section.

In Fig. 5 the "crystal growth rates" R are plotted as a function of the concentration; that is, the concentration of the metastable fluid. Each given experimental value for R is an average over at least four subsequently measured growth curves, of which a few examples are given in Fig. 3. Since no absolute intensities were measured, no absolute growth rates are given. The absolute growth rates are directly proportional to those given in Fig. 5, with an unknown proportionality constant. Clearly there is an optimum growth rate at an inter-

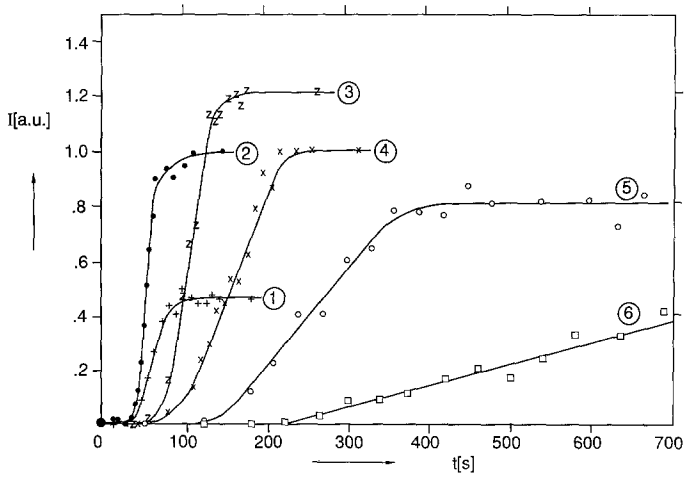

FIG. 3. The scattered intensity I relative to that at $t = 0$ as a function of time for samples with different mean concentrations. The intensity that is plotted is orientationally averaged (by rotation of the cuvette during the experiment) and is integrated over the (111)-Bragg peak intensities which are detected by the linear diode array camera. The mean concentrations are 1 = 0.3790 g/ml (+), 2 = 0.3717 g/ml (●), 3 = 0.3640 g/ml (z), 4 = 0.3581 g/ml (x), 5 = 0.3490 g/ml (○), and 6 = 0.3489 g/ml (□), with an accuracy of 0.0010 g/ml. The full lines are drawn to guide the eye. Each curve is the average of at least four experiments.

mediate concentration. As shown in Fig. 6, however, the induction time is monotonically decreasing with the concentration. At low concentrations it takes a long time before nuclei are formed and subsequently begin to grow. At large concentrations the induction time tends to (35 ± 8) s. Of course, all these trends can be read directly from the growth curves given in Fig. 3. The intensity which is measured after completion of the crystallization process I_f is given in Fig. 7, again as a function of the concentration. The large experimental error for the lower concentrations (despite the increase of the scattering volume and averaging over many measurements) is a result of the large variation of the intensity over the Debye–Scherrer ring. This increasing variation of the intensity over the Debye–Scherrer ring is the result of increasing size and decreasing number density of crystallites. From the full width in scattering angle of the Bragg peaks at half their height, $\Delta\theta_s(\frac{1}{2})$, which is plotted in Fig. 8 as a function of the concentration, it can be deduced that the size of the crystallites increases as the concentration is lowered. To measure the width of the peaks, the cuvette is rotated so that a single Bragg peak hits the diode array. The peak intensity of a Bragg peak as detected by the diode array is maximized by rotation of the cuvette, after

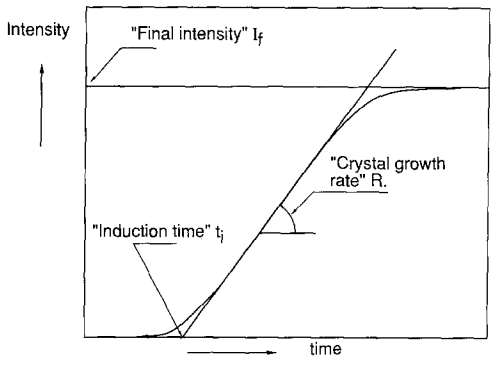

FIG. 4. Schematic growth curve. Three characteristic quantities are defined here: (i) the crystal growth rate R is the slope of the curve at the inflection point, (ii) the induction time t_i is the intersection of a straight line with slope R through the inflection point with the time axis, and (iii) the final intensity I_f is the asymptotic limit of the curve.

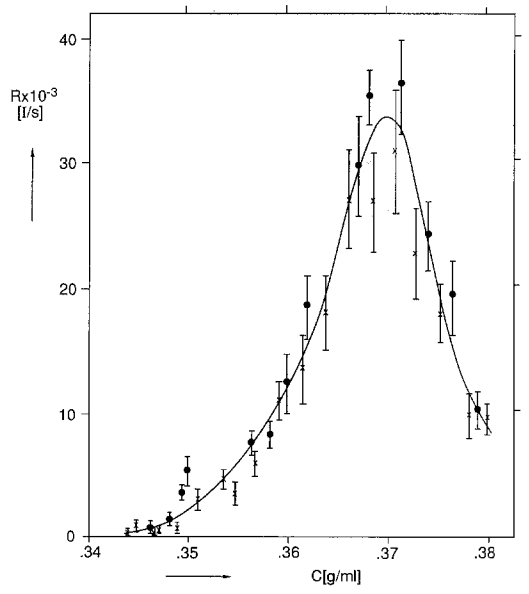

FIG. 5. Crystal growth rates R (as defined in Fig. 4) as a function of the mean concentration. The full line is the best fit by eye. ● and x are results of two independent sets of experiments.

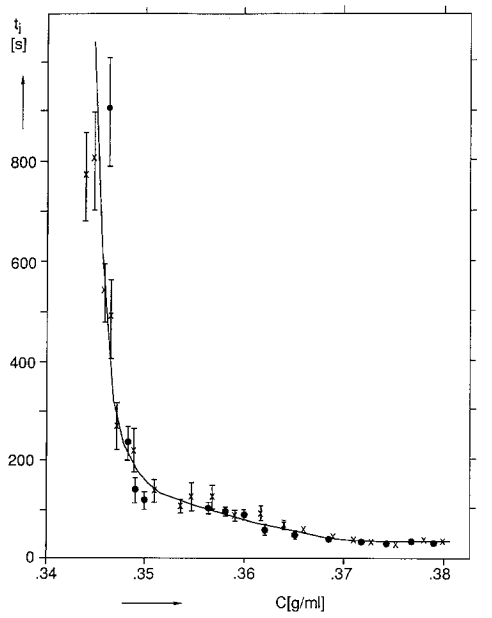

FIG. 6. The induction time (as defined in Fig. 4) as a function of the mean concentration. The full line is the best fit by eye. ● and x are results of two independent sets of experiments.

which the width in scattering angle at half the peak intensity is determined. Each point in Fig. 8 is the average width of Bragg peaks of at least 10 different crystallites. For three different concentrations, measured Bragg peaks are given in Fig. 9. Below $c \approx 0.354$ g/ml, crystallites are so large that it became impossible to accurately rotate the cuvette as needed to find the optimum for the scattered intensity at the maximum of the Bragg peak. Crystallite sizes exceeded 1 mm at concentrations lower than $c \approx 0.354$ g/ml. Using a convex lens, crystallite sizes could be measured directly. The two arrows in Fig. 8 indicate the results of these measurements.

In our search for (111)-Bragg peaks, we found that the scattering angle at which they occurred varied some 2°. All these peaks are (111)-Bragg peaks, as the other Bragg peaks (like the (200)-Bragg peak) are located at scattering angles that differ from that of the (111)-Bragg peak by much more than the angular range spanned by the diode array. This variation of positions of (111)-Bragg peaks

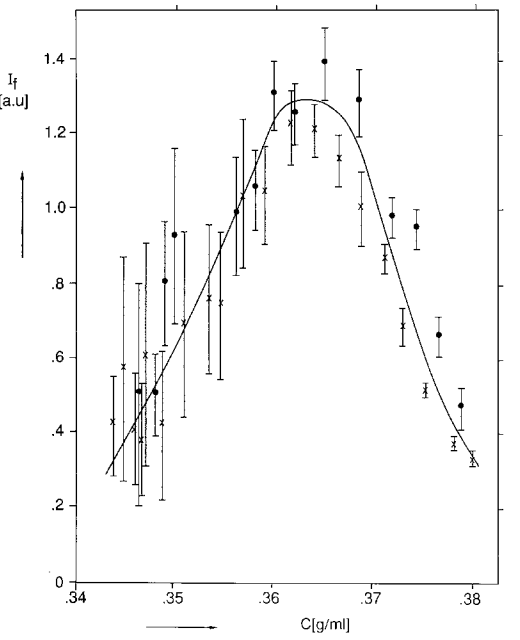

FIG. 7. The final intensity (as defined in Fig. 4) as a function of the mean concentration. The full line is the best fit by eye. ● and x are results of two independent sets of experiments.

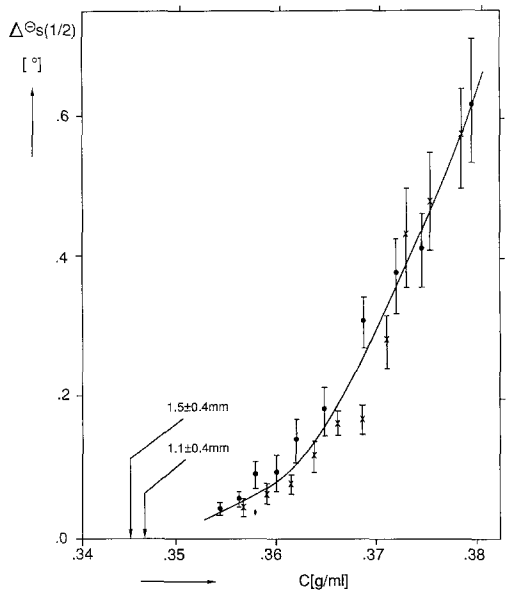

FIG. 8. The width of the (111)-Bragg peak in terms of the scattering angle width at half the peak height as a function of the mean concentration. ● and x are results of two independent sets of experiments. Below $c \approx 0.354$ g/ml, crystals are so large that it was not possible to accurately rotate the cuvette so that the Bragg peak gave rise to an optimum peak- intensity. The arrows indicate sizes which were simply measured geometrically with the aid of a convex lens.

was not an artifact of optical misalignment. The refractive index of the thermostating fluid was refractive index-matched up to the fourth decimal place with that of the dispersion. A deliberate mismatch of ~0.04 in refractive index, by using toluene as the thermostating fluid, had no significant influence on the spread in the observed positions of the Bragg peaks. Furthermore, no significant influence of a small deliberate divergence or convergence of the incident laser beam was detected. It seems that on top of the broad structure factor peak of a metastable fluid, Bragg peaks start to appear at random scattering angles over a range of about 2°. A time-resolved experiment is shown in Fig. 10, where a convex lens is used to enlarge the total scattering range which is detected by the diode array chip to 5.5°, to enable detection of the entire structure factor peak of the metastable fluid. The figure shows the growth of two (111)-Bragg peaks at different scattering angles on top of the structure factor peak of the metastable fluid. The rotational position of the cuvette was not changed

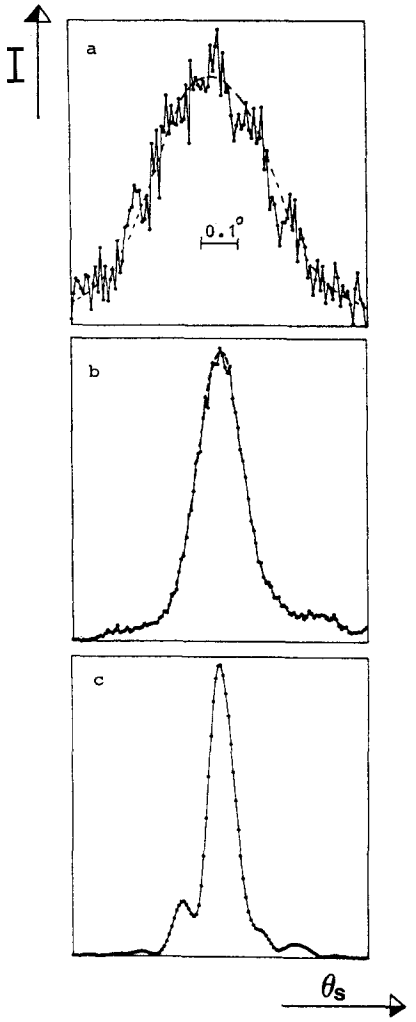

FIG. 9. (111)-Bragg peaks at a mean concentrations of a = 0.3717, b = 0.3640, and c = 0.3581 g/ml. θ_s is the scattering angle and I is the scattered intensity. The experimental intensities ● are connected by straight lines. In Figs. 9a and b the dashed line is the best fit by eye. The scattered intensities in these figures are normalized (approximately) to the maximum intensity. In Fig. 9a the absolute value of the scattered intensity is low, and therefore the scatter in the experimental points is large. The scattering angle is in each case about 75°. In Fig. 9a the scattering angle scale is indicated.

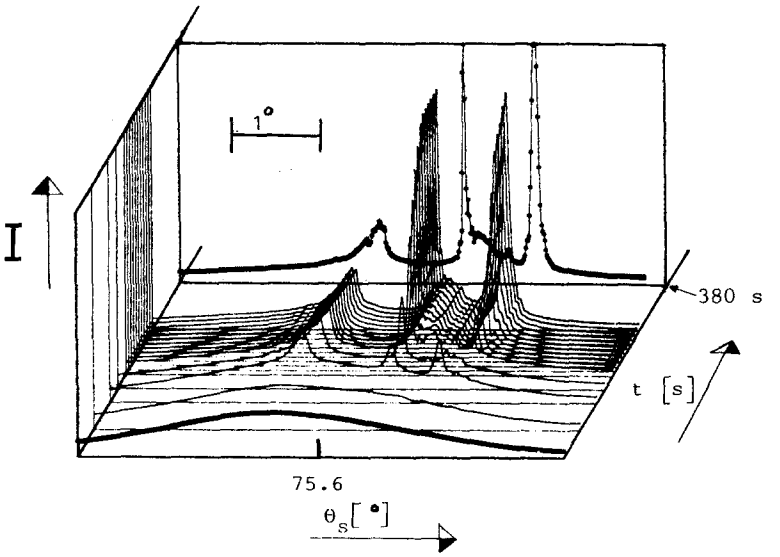

FIG. 10. The scattered intensity I as a function of the scattering angle θ_s and the time t. In this experiment the cuvette was not rotated. A convex lens between the thermostating bath and the camera (GR and DAC in Fig. 2) was used to increase the scattering angle range somewhat. For clarity experimental points are only displayed in the first and the last experiments. In all curves, experimental points are connected by straight lines. The upper horizontal line in the curve at $t = 380$ s indicates the saturation of the diode array camera. The scattering angle is about 75°, and the angular scale is indicated. The metastable fluid peak in the curve at $t = 0$ is somewhat distorted by the use of the convex lens.

during the experiment. The orientation of two crystallites, by chance, happened to be such that their (111)-Bragg peak hit the detector diode array. Note that neither of the two peaks changes its position during the entire growth process. Each Bragg peak starts off with a certain Bragg spacing, which does not change during the entire crystallization process. Part of the time-dependence in this figure, however, may be due to sedimentation; that is, some of the increase in the Bragg-peak intensities may be due to sedimentation of the two crystallites into the scattering volume.

5. ANALYSIS OF THE EXPERIMENTAL RESULTS

To obtain quantities that are directly related to the nucleation/crystallization process from the light-scattering results as presented in the previous section, a model is needed to calculate the intensity and the width of the scattering peak for a single crystallite. In the literature on X-ray diffraction (16), much attention has been paid to this subject. The results of that work also apply to optical diffraction experiments. We can therefore use the relevant formulas derived for X-ray diffraction from crystals.

A nucleating/crystallizing system is a collection of nuclei and polydisperse crystallites. The polydispersity in crystallite sizes is a result of the continuous germination of nuclei.[2] Nuclei are being formed at several instances, with a rate that is most probably proportional to the instantaneous volume of mother fluid; that is, the volume of the entire system minus the volume that is occupied by the nuclei and

[2] In an MD computer simulation study, Cape *et al.* (9) found that the polydispersity in the linear dimension of the nuclei was about 3%. This is an indication that the polydispersity of nuclei is not the origin of the polydispersity in crystallite sizes.

crystallites, with the inclusion of their depletion zones. To take this polydispersity into account in the interpretation of the light-scattering growth curves requires a model for the nucleation rate, nucleus size, crystal growth rates, and the geometry of crystallites, including the stages where different crystallites interfere. As far as we know there is no adequate theory available to implement such an analysis for our experiments. We can only hope that at the stages where a nonzero intensity is measured, nucleation rates are small and crystallites had enough time to grow, and thus to restore the initial relative size polydispersity significantly. At least in the final stages of the crystallization process, the relative polydispersity in crystallite sizes seems to be small, both by visual inspection and by the fact that the spread in measured Bragg peak widths is not large, as indicated in Fig. 8. In the following we will assume uniform crystallite sizes. Furthermore, we assume a cubic form containing $N \times N \times N$ cubic FCC unit cells as a model for our crystallites. Diffusive broadening of the (111)-Bragg peak may be safely neglected, since the Debye–Waller factor is virtually constant over the entire Bragg peak, due to the quite large sizes of the crystallites.

5.1. *Sizes of the Crystallites*

The width and the intensity of the scattering peak in powder X-ray techniques are calculated as averages over the orientation of a crystallite. In our experiments, to obtain the width of scattering peaks, we do not measure an average over orientations, since a single crystallite in the scattering volume is selected; that is, the measured Bragg peak in our case is that of a single crystallite having a fixed orientation, which satisfies the Bragg condition with respect to the diode array chip. For the (111)-reflection, assuming the above mentioned crystallite geometry, we obtain the relation between the full width at half the peak maximum (in degrees), $\Delta\theta_s(\frac{1}{2})$, and the linear dimension L of a crystallite[3]

$$\Delta\theta_s(1/2)[^\circ] = \frac{23.5}{L\,[\mu\mathrm{m}]}. \qquad [5.1]$$

The number of unit cells along the edges of the cubic crystallites is now found from

$$N = \frac{L}{2\sqrt{2}a}, \qquad [5.2]$$

where $2a$ is the shortest distance between two particles in the crystallite, which in turn is found from the scattering angle θ_m at which the (111)-Bragg peak is located, via

$$K_m = \frac{4\pi}{\lambda}\sin(\theta_m/2) = \frac{\sqrt{(3/2)}\,\pi}{a}, \qquad [5.3]$$

where λ is the wavelength of the light in the solvent. Using $\theta_m = 75°$, it is found that $a = 219$ nm. The number of Brownian particles per crystallite now simply follows from [5.2],

$$\mathcal{N} = 4N^3 = \frac{\sqrt{2}L^3}{8a^3}, \qquad [5.4]$$

since a single FCC-unit cell contains 4 particles.

The linear dimension L of the crystallites, as calculated from [5.1] and Fig. 8, is plotted in Fig. 11 as a function of the concentration (of the metastable fluid). The size of the crystallites is seen to decrease from about 1.5 mm to 40 μm in the concentration range 0.35–0.38 g/ml. The directly measured sizes are in accordance with results that are calculated from the widths of the Bragg peaks with the use of Eq. [5.1].

The number of Brownian particles per crystallite as a function of the concentration as calculated from [5.4] and the data in Fig. 11 is presented in Fig. 12. The number of particles in a crystallite sharply decreases from about

[3] This relation may be derived directly from Eq. [6] in Ref. (17), giving the intensity scattered by a single crystallite as a function of the distance (his Δs) from the peak maximum. In the calculation of the numerical factor in [5.2], we used values of quantities pertaining to our experiments.

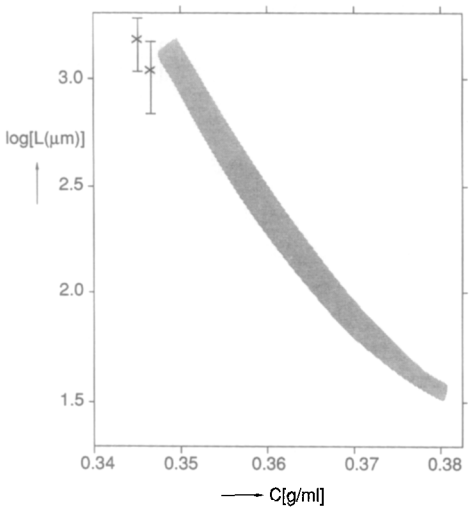

FIG. 11. The length L of the crystals as a function of the mean concentration. The width of the shaded area indicates the error estimate. The two points have been measured directly with a convex lens.

10^{10} to 10^6 in the concentration range 0.35–0.38 g/ml.

5.2. *Number Concentration of Crystallites*

The peak maximum of the (with equal weights) orientationally averaged intensity that is scattered by a cubic crystallite varies with N^4 (16, 17), where N is, as before, the linear dimension of the crystallite in numbers of unit cells. The experimentally measured intensity I_f is the orientationally averaged intensity that is integrated over the scattering angles constituting a straight line, intersecting the peak maximum of the orientationally averaged Bragg peak (this line represents the linear diode array). The resulting line-integrated intensity varies with the number of unit cells as N^3 (17). Since we assumed that all crystallites have the same size, the total intensity I_f from all the crystallites in the scattering volume satisfies

$$I_f \sim N_c N^3, \qquad [5.5]$$

where N_c is the number of crystallites in the scattering volume, which is directly proportional to the number concentration of crystallites in the final stages of the crystallization process, being equal to the total number of nuclei that were formed in the course of the crystallization process. Since I_f was not measured in absolute units, N_c is also obtained up to a proportionality constant. N_c can be calculated from the experimental results using

$$N_c \sim I_f/N^3 \sim I_f(\Delta\theta_s(1/2))^3. \qquad [5.6]$$

Here we used [5.5] together with [5.1], [5.2]. In Fig. 13 the number of crystallites in the scattering volume, N_c, is presented as a function of the concentration. This quantity increases four orders of magnitude in the concentration range 0.35–0.38 g/ml.

5.3. *Rate of Crystal Growth*

A fundamental quantity for the rate of crystal growth is the rate at which the linear dimension of crystallites increases. This quantity is proportional to dN/dt, and is related to the experimental "crystal growth rate" R as

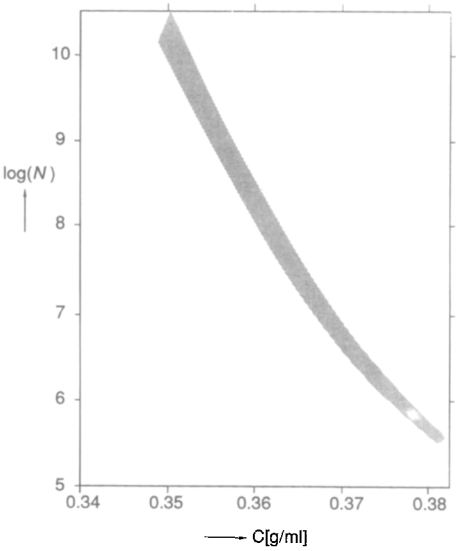

FIG. 12. The average number of particles N in one crystallite as a function of the mean concentration of the particles. The width of the shaded area indicates the error estimate.

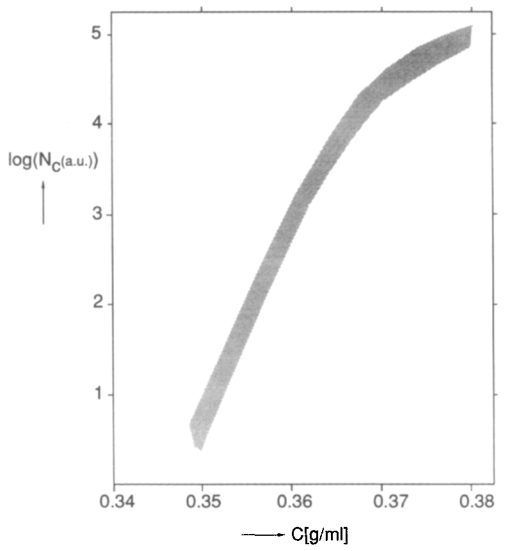

FIG. 13. Number of crystallites in the scattering volume N_c as a function of the mean concentration of the colloidal particles. The width of the shaded area indicates the error estimate.

$$R \sim N_c \frac{dN^3}{dt} = 3N_c N_{1/2}^2 \frac{dN}{dt}, \quad [5.7]$$

where $N_{1/2}^3$ is the number of unit cells per crystallite, at the time when the intensity is equal to $\frac{1}{2}I_f$. If we assume that N_c, for a given concentration, remains constant in time during the crystallization process after the stage where $I = \frac{1}{2}I_f$, it follows that

$$N_{1/2}^3 = 1/2N^3, \quad [5.8]$$

where, as before, N^3 is the number of unit cells per crystallite after completion of the crystallization process. Combination of these two formulas, together with [5.1], [5.2], and [5.5], omitting all proportionality constants, yields

$$\frac{dN}{dt} \sim \frac{R}{N_c N^2} \sim \frac{R}{I_f \Delta\theta_s(1/2)}. \quad [5.9]$$

As before, this expression contains only quantities that have been measured experimentally. In Fig. 14 dN/dt is plotted as a function of the concentration. Clearly this quantity varies very much less drastically with the concentration than all the other quantities calculated so far. Contrary to what is expected (11), this quantity does not increase with concentration for lower concentrations. This may be due to the roughness of the calculations and partly due to experimental errors.

5.4. *Rate of Nucleation*

The number of nuclei that germinate per unit time, the nucleation rate R_n, may be estimated from

$$R_n = N_c/t_i \sim I_f(\Delta\theta_s(1/2))^3/t_i, \quad [5.10]$$

where N_c is the total number of nuclei which are being formed during the crystallization process and t_i is the induction time. In the second step in [5.10] we used [5.6]. Figure 15 gives the nucleation rate as a function of the concentration. Again, this is a quantity which varies dramatically (about five orders of magnitude) in the concentration range 0.35–0.38 g/ml.

6. DISCUSSION AND CONCLUSIONS

With our experiments we have been able to obtain the concentration dependence of various quantities which characterize the nucleation/crystallization process: the induction time, the nucleation rate, the rate of crystal growth, the sizes of crystallites, and the number of crystallites (c.q. the total number of nuclei) that are formed. To relate scattered intensities to quantities that characterize the

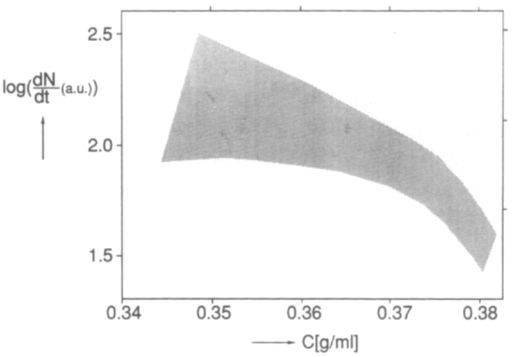

FIG. 14. Rate of growth of one crystal dN/dt as a function of the mean concentration of the colloidal particles. The width of the shaded area indicates the error estimate.

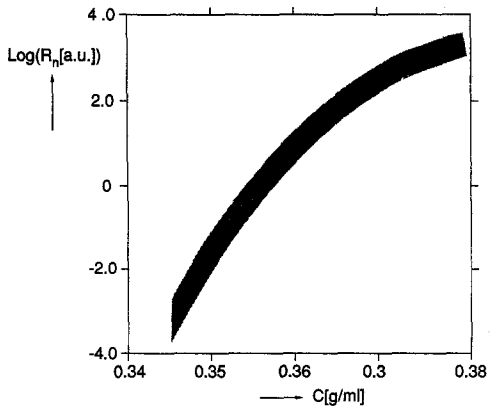

FIG. 15. The nucleation rate, calculated as N_c/t_i, as a function of the concentration. The width of the shaded area indicates the error estimate.

crystallization process, one has to make assumptions about the geometry of the crystallites and their size distribution. Here we used for the geometry of the crystallites a cube of $N \times N \times N$ FCC unit cells, and assumed monodispersity in sizes. The (111)-planes are thus on the diagonal of the cubes. These approximations will allow for conclusions on clear-cut concentration dependencies only. If a quantity is calculated with the use of these approximations, and turns out to be only weakly dependent on the concentration as a result of cancellation of terms, one should keep in mind that this concentration dependence may be determined to a large extent through the approximations that are involved. The inaccuracy of the approximations does not allow for a detailed interpretation of the results in those cases. The crystal growth rate (Fig. 14) should therefore be interpreted with some care. The sizes of the crystallites are found to be so large that the Debye–Waller factor is constant over the entire (111)-Bragg peak, so that diffusive broadening of the measured Bragg peaks may safely be neglected.

In the previous section we found that the location of the (111)-Bragg peak corresponds to a shortest center-to-center distance of the spherical Brownian particles of $2a = 2 \times 219$ nm. When a is used as an effective hard-core radius, effective hard-core volume fractions may be defined by rescaling the true hard-core volume fraction by a factor $(219/160)^3$, where 160 nm is the true hard-core radius of the particles. These rescaled effective volume fractions ϕ_{hs}^{eff} are indicated in the phase diagram in Fig. 1. The effective freezing volume fraction thus obtained (0.497) is very close to that of a hard-sphere system (0.494) as found by computer simulation (18). The melting volume fraction for hard spheres is 0.545. Therefore, we expect that the melting concentration of the TPM-silica is about 0.372 g/ml. This is very close to the concentration where the experimental crystal growth rate R, as defined in Fig. 4, has a maximum as a function of the concentration (see Fig. 5), in accordance with findings by Pusey and van Megen (6). Note that the rescaled hard-core volume fraction where crystallization no longer occurs over extended periods of time (0.574) is smaller than the volume fractions for the hard-sphere glass transition points (~0.64–0.66) (see Ref. (6) and references therein). Either the system is still fluid-like or rescaling to an effective hard sphere does not work for the glass transition, possibly because the glass transition is related to the dynamics rather than to the thermodynamics of the system.

We find that the induction time decreases with increasing concentration, or equivalently, with increasing supersaturation, and asymptotically approaches a finite time (35 ± 8 s) in the concentration range where only homogeneous nucleation occurs. The theoretical work of Russel (11), where classical nucleation and growth theories are adapted for colloidal systems, predicts that for hard spheres the rate of nucleation increases about 50 orders of magnitude in the volume fraction range 0.52–0.56. Taking N_c/t_i as a measure for the rate of nucleation, we find that the rate of nucleation increases about five orders of magnitude in the concentration range 0.35–0.38 g/ml (see Fig. 15). As was discussed above, this concentration range may be mapped onto an effective hard-sphere volume fraction range of 0.513–0.557. The increase in nucleation rates with the concentration that we find for the

slightly charged TPM-particles is quite drastic, but far less drastic than is predicted by Russel for hard spheres.

We observe that the size of the crystallites monotonically decreases with the concentration over the entire concentration range, which is partly located between the freezing and melting point. Pusey and Van Megen (6) also observed, by eye, such a monotonic decrease in crystallite size, except in the coexistence region, where the crystallites appeared to have a concentration-independent size. As pointed out by these authors, however, the latter observation could be due to sedimentation. Russel (11) predicts theoretically, and Cape *et al.* (9) find by computer simulation, that the sizes of the *nuclei* decrease many orders of magnitude with increasing concentration. Since the crystallite growth rate (Fig. 14) is not so drastically concentration-dependent as the sizes of nuclei and nucleation rates, the concentration dependence of the nuclei sizes may be the origin of the concentration dependence that we find for the *crystallite* sizes after completion of the crystallization process.

The experimentally observed rate of crystal growth R shows a maximum as a function of the concentration (Fig. 5). As we mentioned before, a similar observation was made by Pusey and van Megen (6) for a nearly hard-sphere system. They estimated the time of formation of crystals by measuring the time elapsed after randomizing the suspension until, for the first time, crystals could be seen. This time actually includes the induction time, so that this time is only a proper measure for the growth rate of crystallites whenever the induction time varies much less pronounced with the concentration than R itself. From Fig. 6 it can be seen that, for the charged TPM-silica, this is only the case for concentrations larger than say 0.355 g/ml, corresponding to an effective hard-core volume fraction of 0.52. Since the melting volume fraction for hard spheres is 0.545, quite a bit larger than 0.52, the maximum in the crystal growth rate R at the melting concentration as observed in Ref. (6) is in accord with our findings.

We observe that the growth rate of the interface of crystallites, as expressed by dN/dt, is decreasing with the concentration for larger concentrations (Fig. 14). This is contrary to earlier experimental work of Aastuen *et al.* (7) on very dilute systems with a long Debye screening length, where the growth rate is seen to increase monotonically with the concentration. However, Russel (11) argues that the crystal growth rate at larger concentrations is determined by the behavior of the self-diffusion coefficient that limits the assumed diffusion-controlled crystal growth. For the highly charged spheres used by Aastuen, the self-diffusion coefficient is independent of the concentration and equal to the Stokes–Einstein diffusion coefficient, and Russell indeed finds a monotonically increasing crystal growth rate in this case. For the more concentrated systems where hydrodynamic interactions diminish the self-diffusion coefficient, he finds an optimum in the crystal growth rate as a function of the concentration (see also Ref. (10)). The different behavior of the crystal growth rate as a function of the concentration for the system investigated by Aastuen *et al.* and in the present paper is thus most probably due to the different behavior of the diffusional properties of the Brownian particles at larger concentrations. The crystal growth rates that are presented in Fig. 14 are only weakly concentration-dependent due to a cancellation of concentration dependencies of terms that are obtained from the light-scattering experiments and our simple monodisperse cubic crystallite geometry model. The fact that Fig. 14 does not show a marked maximum, as one would expect on the basis of Russel's work (11), is, besides experimental inaccuracies, probably the result of the crudeness of this model (see the discussion at the beginning of this section). Direct observation of the interface of a single crystallite is a more reliable and more direct way to determine the interfacial velocity, as is done in Ref. (7) for highly charged particles.

The number of crystallites (c.q. the total number of nuclei that were formed during the crystallization process) and the crystallite size

is found to be rapidly increasing (Fig. 13), respectively decreasing (Figs. 11 and 12), with increasing concentration. This is due to the rapidly increasing nucleation rates with concentration (Fig. 15), since the crystal growth rate is only weakly concentration-dependent (Fig. 14).

The (111)-Bragg peak location is somewhat different for different crystallites. The spacing between the (111)-layers is thus not exactly the same for all crystallites. Two possible explanations are: (i) once a nucleus is formed, part of the nonideality of its structure is preserved during its growth into a crystallite, and (ii) concentration fluctuations that lead to the formation of a nucleus select Brownian particles with a size polydispersity that is smaller than the average size polydispersity (6%), so that each nucleus consists on average of different sized Brownian particles, and this size difference is maintained, in part, during growth.

ACKNOWLEDGMENTS

It is a pleasure to thank Drs. P. Buining (University of Utrecht) and P. Mast (DSM, Geleen) for performing the electrophoretic measurements. These experiments were done at DSM, Geleen, The Netherlands.

REFERENCES

1. Hachisu, S., and Takano, K., *Adv. Colloid Interface Sci.* **16,** 233 (1982).
2. Kirkwood, J. G., *J. Chem. Phys.* **7,** 919 (1939).
3. Alder, B. J., and Wainwright, T. E., *J. Chem. Phys.* **27,** 1208 (1957).
4. Monovoukas, Y., and Gast, A. P., *J. Colloid Interface Sci.* **128,** 533 (1989).
5. Pusey, P. N., and van Megen, W., *Nature* **320,** 340 (1986).
6. Pusey, P. N., and van Megen, W., *in* "Physics of Complex and Supermolecular Fluids" (S. A. Safran and N. A. Clark, Eds.). Wiley–Interscience, New York. 1987.
7. Aastuen, D. W. J., Clark, N. A., Cotter, L. K., and Ackerson, B. J., *Phys. Rev. Lett.* **57,** 1733 (1986).
8. Davis, K. E., and Russel, W. B., *Ceram. Trans. B* **1,** 693 (1988).
9. Cape, J. N., Finney, J. L., and Woodcock, L. V., *J. Chem. Phys.* **75,** 2366 (1981).
10. Davis, K. E., and Russel, W. B., *Adv. Ceram.* **21,** 573 (1987).
11. Russel, W. B., to be published.
12. Philipse, A. P., and Vrij, A., *J. Colloid Interface Sci.* **128,** 121 (1989).
13. Hunter, R. J., *in* "Zeta Potential in Colloid Science" (R. H. Ottewill and R. L. Rowell, Eds.). Academic Press, New York, 1981.
14. Loeb, A. L., Overbeek, J. Th. G., and Wiersema, P. H., "The Electrical Double Layer Around a Spherical Colloid Particle." MIT Press, Cambridge, MA, 1961.
15. Philipse, A. P., and Vrij, A., *J. Chem. Phys.* **88,** 6459 (1988).
16. James, R. W., "The Optical Principles of the Diffraction of X-Rays. The Crystalline State" (L. Bragg, Ed.), Vol. II. Cornell Univ. Press, Ithaca, NY, 1965.
17. Warren, B. E., *Z. Kristallogr.* **99,** 448 (1938).
18. Hoover, W. G., and Ree, F. H., *J. Chem. Phys.* **49,** 3609 (1968).